

High-Integrity Surface Navigation for Unmanned Aircraft: A Multi-Frequency GNSS Approach

Daniel J Larimer, *Illinois Institute of Technology*
Dr. Samer Khanafseh, *Illinois Institute of Technology*
Dr. Kana Nagai, *Illinois Institute of Technology*
Dr. Boris Pervan, *Illinois Institute of Technology*

Biographies

Daniel Larimer is a Research Engineer in Mechanical and Aerospace Engineering at Illinois Institute of Technology (IIT). He received a B.S. in Aerospace Engineering from IIT and a B.S. in Liberal Arts Engineering from Wheaton College. He works on high-accuracy and high-integrity navigation systems for autonomous vehicles.

Dr. Samer Khanafseh is currently a Research Associate Professor at the Illinois Institute of Technology (IIT) and the Principal of TruNav LLC. He received his M.S. and Ph.D. degrees in Mechanical and Aerospace Engineering from IIT in 2003 and 2008, respectively. His work has involved several aviation applications, including Autonomous Airborne Refueling (AAR) of unmanned aerial vehicles, autonomous shipboard landing for the NUCAS and JPALS programs, and the Ground-Based Augmentation System (GBAS). His research interests are focused on high accuracy and high integrity navigation algorithms, cycle ambiguity resolution, high integrity applications, fault monitoring and robust estimation techniques. He was the recipient of the 2011 Institute of Navigation Early Achievement Award for his outstanding contributions to the integrity of carrier phase navigation systems.

Dr. Kana Nagai is a Senior Research Associate in the Department of Mechanical and Aerospace Engineering at the Illinois Institute of Technology (IIT). She holds M.S. and Ph.D. degrees in Mechanical and Aerospace Engineering, as well as a B.S. in Mechanical Engineering, all from IIT. Additionally, she earned a B.E. in Architecture from Hokkaido University in Japan.

Dr. Boris Pervan is a Professor and Frank Gunsaulus Faculty Fellow in Mechanical and Aerospace Engineering at the Illinois Institute of Technology (IIT), where he conducts research on high integrity navigation systems. Prior to joining the faculty at IIT, he was a spacecraft mission analyst at Hughes Aircraft Company (now Boeing) and a postdoctoral research associate at Stanford University. Prof. Pervan received his B.S. from the University of Notre Dame, M.S. from the California Institute of Technology, and Ph.D. from Stanford University. He has received the Samuel M. Burka and Johannes Kepler Awards from the Institute of Navigation (ION), IIT Sigma Xi Excellence in University Research Award (twice), IIT University Excellence in Teaching Award, IEEE Aerospace and Electronic Systems Society M. Barry Carlton Award, RTCA William E. Jackson Award, Guggenheim Fellowship (Caltech), and the Albert J. Zahm Prize in Aeronautics (Notre Dame). He is a Fellow of the ION and former Editor-in-Chief of the ION journal NAVIGATION.

ABSTRACT

The aviation landscape is undergoing a rapid shift as advanced automation transforms not only unmanned aircraft, but also conventional platforms enhanced with pilot-assist or semi-autonomous functions. Despite decades of research and development, there is currently no safety-assured system capable of performing automatic takeoff, landing, and taxiing. In the past two decades, automatic approach and landing have seen significant technological development, while limited research and development in surface operations has left a critical void in technological readiness for UAS integration. This study proposes a navigation system architecture capable of filling the technical gap in autonomous aircraft surface operations. The analysis begins by identifying the scope of operations and the stringent accuracy requirements that the system will be expected to meet. Regulatory authorities are proactively shaping standards for autonomous surface operations, and meeting these evolving benchmarks is essential for the operations of any automated or assisted aircraft. In this work, we present a multi-frequency, multi-constellation differential GNSS architecture for automated and semi-autonomous aircraft surface operations, focusing on

stringent integrity, continuity, and accuracy requirements. This approach builds on Ground-Based Augmentation System Approach Service Type E (GAST-E) inspired concepts to address this critical gap preventing seamless integration of Unmanned Aircraft System into the National Airspace System. We demonstrated through use of covariance analyses that even with significant satellite blockages from airport infrastructure, the system is capable of meeting the given requirements under fault-free conditions. Sensitivity analysis demonstrates that the system performance is highly impacted by the multipath environment, satellite blockage, and implementation of a zero-velocity update.

1. INTRODUCTION

The integration of Uncrewed Aircraft Systems (UAS) and pilot-assist functions into the National Airspace System (NAS) offers exciting opportunities for the future of aviation, while also presenting unique challenges. With much research and development being poured in autonomous approach landing leading to significant technological development, the need for a system that can provide autonomous surface operation for UAS has never been greater. Although there are significant challenges presented by the high accuracy required on narrow runways, satellite blockages caused by airport infrastructure, multipath effects present in the airport environment, and the integrity required for safety-of-life systems, in this study we demonstrate these challenges can be bridged to form a viable solution.

In aviation, demonstrating the ability of any UAS to meet required accuracy, integrity, continuity, and availability requirements (Davis and Kelly, 1993) is critical to its safe operation and viability. Accuracy is the ability of the UAS to maintain the aircraft position within a total system error (TSE) bound. The TSE can be further budgeted into path definition error (PDE), flight technical error (FTE), and navigation system error (NSE). Integrity quantifies the reliability of the information from the navigation system and alerts the user if the information from the system falls outside the bounds of a certain reliability. Continuity measures the probability that the navigation system will be interrupted during the operation. Availability measures the likelihood that the system will meet the accuracy, integrity, and continuity requirements throughout the operation. If a system is insufficient in any of these four areas, the viability and safety of that system are compromised.

Although limited research has been given to the application of GNSS for high integrity UAS surface operations, one study demonstrated that differential GNSS can satisfy the integrity and accuracy requirements for surface movement from landing to the stand-in line at class-F airports. The study applied an Extended Kalman Filter (EKF) that tightly coupled carrier smoothed GNSS measurements and INS measurements, followed by Relative Receiver Autonomous Integrity Monitoring (Song, 2024).

In this paper, we suggest a navigation architecture that enhances a differential EKF with geometry-free divergence-free filtering and the use of both code measurements and carrier phase measurements, enabling fault-free integrity and accuracy requirements to be met for surface operations at any airport, for both arrival scenarios and departure scenarios. Additionally, a detailed sensitivity analysis identifies specific error sources that significantly affect system performance.

Following this introduction, Section II outlines the accuracy and fault-free integrity requirements. Section III describes system architecture, while Section IV presents the covariance analysis. Section V focuses on the sensitivity analysis, and Section VI concludes the paper with a summary of future work.

2. ACCURACY AND FAULT-FREE INTEGRITY REQUIREMENTS

To develop a navigation system that enables autonomous surface operations, a clear understanding of the accuracy and integrity requirements is needed. However, with renewed research into UAS surface operations, the requirements to certify an autonomous taxiing system are still undergoing review by the Radio Technical Committee for Aeronautics (RTCA). Until requirements are finalized, the work of designing a navigation system can be based on an examination of what the requirements are expected to entail.

Performance requirements for GNSS in surface operations were first drafted in DO-247 by the RTCA. The scope of surface operations can be separated into arrival and departure operations. The RTCA further divided arrival operations into several phases: rollout, high speed taxi, normal taxi, taxi lane, standing, and docking. As shown in Figure 1, departure operations can also be divided into standing, taxilane, normal taxi, takeoff roll, and liftoff phases (RTCA, 1999).

When considering surface operations, the accuracy requirements in the lateral direction drive the requirements for the system. While taxiing, the aircraft must remain within a containment limit, which is the allowable distance an aircraft may deviate laterally from its desired path. Aircraft and airports are divided into Airplane Design Groups (ADG) and corresponding Taxiway Design Groups (TDG) based on the size of the aircraft's main gear and wingspans. Since rollout is handled by autonomous landing systems, gate entry and exit require coordination with other vehicles, this paper focuses on the positioning

systems for aircraft operating on **taxiways** and **taxilanes**. This includes the time when the arriving aircraft exits the runway until it is ready to park, and the time when the departing aircraft begins forward motion after departing the gate until it arrives at the runway for takeoff.

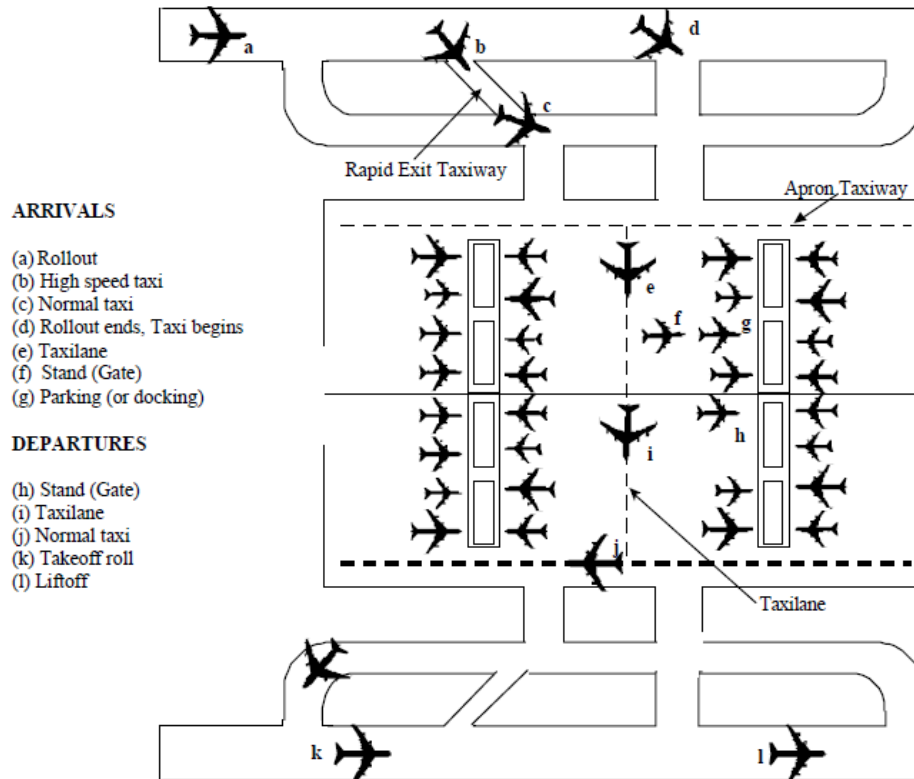


FIGURE 1 Aircraft Phases of Operation (RTCA, 1999)

For a given TDG/ADG, the containment limits for the taxiways, taxilanes, and stand locations provide a certain margin of lateral movement. This margin will differ between taxiways and taxilanes within the same airport code and will also differ between airports. For taxiways, the driving constraint is the margin between the main gear and the taxiway edge, but for taxilanes, the margin between the wingtip and the nearest object is also considered. Although taxiways and taxilanes are required to have the same margins between the main gear and the edge of the designated path, taxilanes have a lower margin for wingtip clearance than do taxiways. To conservatively account for the added risk, the taxilane margin will be multiplied by the ratio of the wingtip clearance for taxilanes to that for taxiways, displayed in Equation 1 (Schuster, 2011).

$$\text{Taxilane Derived Safety Margin} = \text{Taxiway Edge Safety Margin} \left(\frac{\text{Taxilane Wingtip Clearance}}{\text{Taxiway Wingtip Clearance}} \right) \quad (1)$$

The taxiway and taxilane widths for a given TDG/AGD are presented on the table below (U.S. Department of Transportation, Federal Aviation Administration [FAA], 2024).

TDG / AGD	Taxiway Edge Safety Margin (m)	Taxilane Wingtip Clearance / Taxiway Wingtip Clearance (m)	Derived Taxilane Safety Margin (m)
1A/1B	1.5	4.6 / 6.1	1.12
2A/2B	2.3	4.7 / 6.9	1.58
3	3	6.1 / 8.1	2.26
4	3	8.1 / 11.0	2.37
5	4.3	8.5 / 10.8	3.39
6	4.3	9.1 / 11.1	3.53

TABLE 1 Taxiway and Taxilane Design Margins (FAA, 2024)

The taxiway and taxilane margins from the table above can be taken to be the TSE allocated to the system. To prove the safety of the system, the probability of the UAS’s position exceeding the TSE must be less than a given probability. This paper follows the example of previous research by assuming that probability is the same 1×10^{-6} /operation requirement that is used for CAT-III landings (Schuster, 2011). While this requirement subject to change pending upcoming RTCA guidelines, the given probability seems to be a reasonable estimate. Assuming a Gaussian distribution, TSE can be broken down into Navigation System Error (NSE), Flight Technical Error (FTE), and Path Definition Error (PDE) using the root-sum-square method (RSSM), as shown in Equation 2:

$$TSE^2 = PDE^2 + FTE^2 + NSE^2 \tag{2}$$

According to ICAO annex 14, the taxiway centerlines must be surveyed to an accuracy of 0.5 m with a probability of 1×10^{-5} (International, 1999). Assuming this error follows a Gaussian distribution and increasing the error margin to match the 1×10^{-6} value for CAT-III landings, we can assume the taxiway centerlines have been surveyed to an accuracy of 0.56 m with a probability of 1×10^{-6} . Allowing this amount to be budgeted to the PDE, the remaining amount of error can be distributed evenly between FTE and NSE, also assuming a probability of 1×10^{-6} . Table 2 presents the requirements for NSE once the taxiway centerlines have been considered, and the remaining allocation has been evenly split.

TDG/ADG	Taxiways		Taxilanes	
	Margin (m)	NSE Allocation (m)	Margin (m)	NSE Allocation (m)
1A/1B	1.5	0.98	1.12	0.69
2A/2B	2.3	1.58	1.58	1.04
3	3.0	2.09	2.26	1.55
4	3.0	2.09	2.37	1.63
5	4.5	3.16	3.39	2.36
6	4.5	3.16	3.53	2.46

TABLE 2 Taxiway and Taxilane NSE Allocation

One difficulty in quantifying FTE is that the values change based on the aircraft and the speed at which they travel. Generally, smaller aircraft have lower FTE, as well as aircraft traveling at slower speeds. Therefore, as the margins decrease from larger to smaller aircraft, and as the aircraft travels from the gate to the taxiway, the FTE will also decrease. Unlike FTE, the NSE is relatively independent of aircraft type. If a navigation system can provide enough accuracy to meet the NSE allocation while at the gate of a TDG 1A or 1B airport, the same system will not need to take any more budget if implemented on the taxiways of an ADG 6 airport. Therefore, designing the navigation system must be an iterative process: first determine the required NSE accuracy, then design the system according to those requirements, evaluate the performance of the system, and finally decide whether the NSE is sufficient or if further improvement of the navigation system is needed. Additionally, the lower the NSE drops, the more budget can be allocated to FTE to accommodate as many aircraft as possible.

We must implement a navigation system that has a probability of exceeding the lateral limits to be less than 1×10^{-6} per operation. For fault-free analysis, 10% of the probability is arbitrarily allocated to the fault-free condition. The remaining 90% of it is allocated to the faulted condition, which will be considered in future work. Accordingly, the fault-free allowance per operation must be divided into a fault-free allowance per test, using a time-to-alert (TTA) value of 2 seconds (RTCA, 1999). Additionally, given that the average surface operation time including departure and arrival is 18.5 minutes, the average amount of tests in an operation is around 555 (RTCA, 1999). Conservatively assuming independent samples of test epochs and dividing the probability of exceedance per operation evenly between each of these instances, the probability of exceedance per test would be 1.80×10^{-10} (Pervan, 2017). Assuming the error is a Gaussian distribution, the standard deviation of the NSE corresponding to 1.80×10^{-10} must be 6.27 times less than the NSE allocation. Table 3 displays the 1σ standard deviation our navigation system must achieve to meet the accuracy requirements and safely position the aircraft given the fault-free conditions.

TDG/ADG	Taxiways		Taxilanes	
	NSE Allocation (m)	NSE Allocation 1 σ (m) / Test	NSE Allocation (m)	NSE Allocation 1 σ (m) / Test
1A/1B	0.98	0.16	0.69	0.11
2A/2B	1.58	0.25	1.04	0.17
3	2.09	0.33	1.55	0.25
4	2.09	0.33	1.63	0.26
5	3.02	0.48	2.36	0.38
6	3.02	0.48	2.46	0.39

TABLE 3 Taxiway and Taxilane NSE Allocation / Test

3. SYSTEM ARCHITECTURE

A robust and safe navigation system for UAS must meet the stringent accuracy requirements described in Table 3. We designed our navigation system to take advantage of and extend the performance to the GAST-E differential correction system that is currently being developed (Felux, 2025). We propose implementing a combination of the following technologies to meet the required performance:

3.1 Differential GNSS

Using a ground station such as GAST-E to broadcast corrections is a reliable way to mitigate many possible sources in the ranging measurements of GNSS. A problem with the ranging signals is that they are subject to error by many possible error sources. Equation 3 displays the pseudorange measurement, where ρ is the measured range, r is the true range, δt is the clock error of the user, $\delta^s t$ is the clock error of the satellite, I is the error introduced by the ionosphere, T is the error introduced by the troposphere, and m is the error introduced by multipath, and ε is the receiver noise.

$$\rho = r + c * \delta t - c * \delta^s t + I + T + m + \varepsilon \quad (3)$$

The receiver clock error can be eliminated through single-differencing where the signal from the i -th satellite is subtracted from the signal of the j -th satellite. Equation 4 displays the equation for a single-differenced signal.

$$\Delta\rho_{ij} = \Delta r_{ij} - c\Delta\delta^s t_{ij} + \Delta I_{ij} + \Delta T_{ij} + \Delta m_{ij} + \Delta\varepsilon_{ij} \quad (4)$$

To eliminate the satellite orbit and clock errors, ionospheric errors, and tropospheric errors, the reference station must have a known location, be near the user and broadcast its measurements to the user. Since the line-of-sight from the user and reference station to a given satellite is nearly identical, the Ionospheric and Tropospheric errors will be nearly the same. By subtracting the single difference calculation of the user from the reference station, a double difference calculation will provide the user with a ranging measurement relative to the reference station's location.

$$\nabla\Delta\rho_{ij}^{ru} = \nabla\Delta r_{ij}^{ru} + \nabla\Delta m_{ij}^{ru} + \nabla\Delta\varepsilon_{ij}^{ru} \quad (5)$$

While the double differencing operation helps to eliminate many of the error sources, it comes at the cost of inflating multipath and receiver noise. The noise for the double difference operation can be described by the following equation:

$$\nabla\Delta\sigma_m^2 = \sigma_{m_i}^2 + \sigma_{m_j}^2 + \sigma_{m_i^u}^2 + \sigma_{m_j^u}^2 \quad (6)$$

$$\nabla\Delta\sigma_\varepsilon^2 = \sigma_{\varepsilon_i}^2 + \sigma_{\varepsilon_j}^2 + \sigma_{\varepsilon_i^u}^2 + \sigma_{\varepsilon_j^u}^2 \quad (7)$$

If we assume that the thermal noise and receiver noise is the same for all satellites and both receivers, we obtain Equations 8 and 9, showing that the double-differencing operation will generally double the multipath and receiver noise.

$$\nabla\Delta\sigma_m = 2 \sigma_m \quad (8)$$

$$\nabla\Delta\sigma_\varepsilon = 2\sigma_\varepsilon \quad (9)$$

3.2 GPS & Galileo Constellations

Currently, differential systems for autonomous approaches and landings rely only on the GPS constellation. The accuracy of a GNSS navigation system can be improved with each subsequent constellation that is implemented. Since implementing more constellations allows for more satellites to be used in the positioning calculation, achieving a lower dilution of precision leads to higher accuracy. Figure 2 displays the horizontal dilution of precision (HDOP) across 24 hours at Fairbanks (64.82° N) for elevation masks of 5°, 20°, and 30°. As can be seen, especially with higher elevation masks, GPS alone is unable to retain low HDOP at a sufficient level of availability.

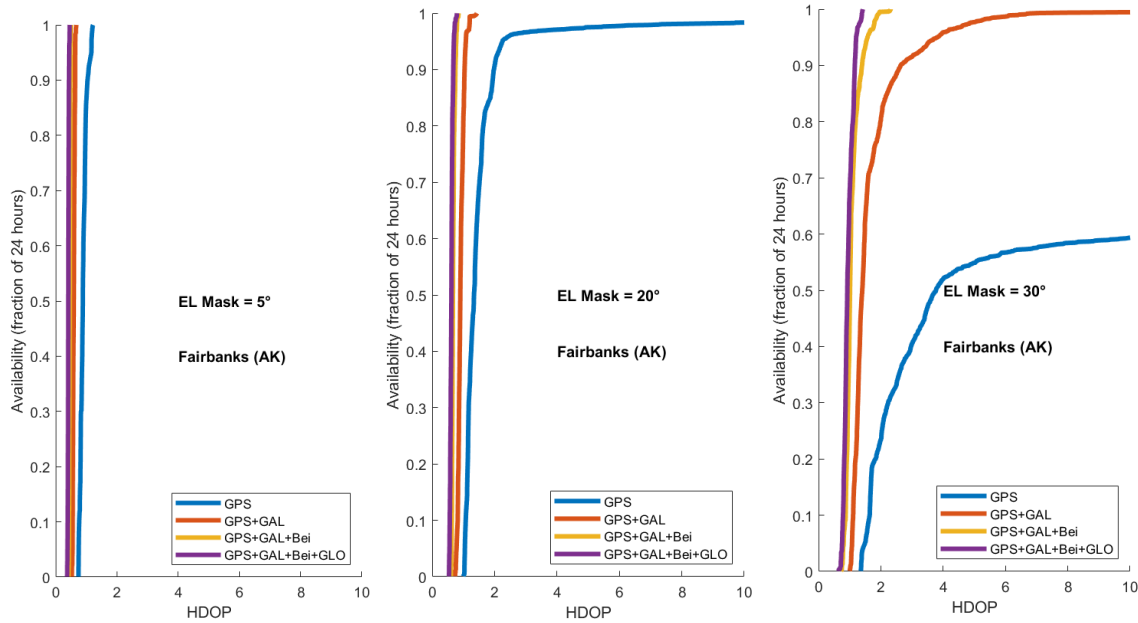


FIGURE 2 Fairbanks HDOP vs Availability for various Elevation Masks

The most straightforward solution might seem to be the use of all constellations, but adding constellations makes evaluating integrity more complicated. We decided to use the Galileo and GPS constellations, which provide enough Dilution of Precision while keeping the system relatively simple.

3.3 L1/L5 & E1E5 Frequencies

With the implementation of the L5 frequency currently underway, the use of both the L1 and L5 frequencies for GPS and the E1 and E5a frequencies for Galileo will provide better accuracy than a single frequency system. An added difficulty for dual frequency systems is the antenna group delay variation (AGDV) caused by antennas processing signals on different frequencies. AGDV is almost indistinguishable from the multipath model, since both are line-of-sight dependent and frequency dependent. If the user has a bad antenna with significant AGDV, combining both error sources into one model can be problematic because AGDV errors are specific to a given antenna (Bang, 2024). This reality will need to be considered when determining what antennas are acceptable for use in UAS operations, and whether the AGDV variation can be considered part of the multipath model or must be examined separately.

3.4 Geometry-Free Divergence-Free Filtering

An added benefit of using multiple frequencies is the ability to use geometry-free divergence-free filtering (GFF). GFF is an approach introduced to obtain better initial information on the carrier phase cycle ambiguities for a multi-frequency differential GNSS navigation system (Heo, 2006; Khanafseh, 2008). The improved initial information allows the user to initialize their EKF to obtain a better positioning estimate much faster. When a user implements code and carrier measurements in an Extended Kalman Filter (EKF), the initial uncertainty on the carrier phase cycle ambiguities is quite large. The longer the EKF processes the measurements, the more it converges, yielding higher accuracy on the cycle ambiguity estimates and therefore on the position state. However, if a UAS does not have access to measurements from the reference station until entering the service

volume and needs a given accuracy to enter the taxiway moments later, a simple initialization of the Kalman Filter upon touchdown is insufficient. GFF is implemented to augment the EKF and allow it to achieve higher accuracy much faster.

The narrow-lane pseudorange, a combination of the L1 and L5 pseudorange signals, can be defined as:

$$\rho_n^i = \left(\frac{\rho_{L1}^i}{\lambda_{L1}} + \frac{\rho_{L5}^i}{\lambda_{L5}} \right) \left(\frac{\lambda_{L1}\lambda_{L5}}{\lambda_{L1} + \lambda_{L5}} \right) \quad (10a)$$

$$= r^i + c * \delta t^i - c * \delta^s t_i^i + \frac{\lambda_{L5}}{\lambda_{L1}} I^i + T^i + \left[\left(\frac{M_{L1}^i}{\lambda_{L1}} + \frac{M_{L5}^i}{\lambda_{L5}} \right) + \left(\frac{\varepsilon_{L1}^i}{\lambda_{L1}} + \frac{\varepsilon_{L5}^i}{\lambda_{L5}} \right) \right] \left(\frac{\lambda_{L1}\lambda_{L5}}{\lambda_{L1} + \lambda_{L5}} \right). \quad (10b)$$

The wide-lane carrier phase, a combination of the L1 and L5 carrier phase signals, can be defined as

$$\phi_w^i = \left(\frac{\phi_{L1}^i}{\lambda_{L1}} - \frac{\phi_{L5}^i}{\lambda_{L5}} \right) \left(\frac{\lambda_{L1}\lambda_{L5}}{\lambda_{L1} - \lambda_{L5}} \right) \quad (11a)$$

$$= r^i + c * \delta t^i - c * \delta^s t_i^i + \frac{\lambda_{L5}}{\lambda_{L1}} I^i + T^i + (N_{L1}^i - N_{L5}^i) \left(\frac{\lambda_{L1}\lambda_{L5}}{\lambda_{L1} - \lambda_{L5}} \right) + \left[\left(\frac{M_{L1}^i}{\lambda_{L1}} + \frac{M_{L5}^i}{\lambda_{L5}} \right) + \left(\frac{\varepsilon_{L1}^i}{\lambda_{L1}} + \frac{\varepsilon_{L5}^i}{\lambda_{L5}} \right) \right] \left(\frac{\lambda_{L1}\lambda_{L5}}{\lambda_{L5} - \lambda_{L1}} \right). \quad (11b)$$

The geometry free measurement Z_{GF} is defined by subtracting the narrow-lane pseudorange (10b) from the wide-lane carrier phase measurement (11a), where λ_w is the wide-lane wavelength, N_w^i is the wide-lane cycle ambiguity, m_{GF}^i is the error due to multipath, and ε_{GF}^i is the error due to receiver noise. Multipath and receiver noise can be modeled as first order Gauss-Markov (FOGM) processes with the variance described in Equation 13. Notice the Ionosphere state is cancelled out in equation 12, meaning the Z_{GF} measurement is divergence-free and can be filtered as long as a lock is maintained on the carrier phase.

$$Z_{GF} = \phi_w^i - \rho_n^i = \left(\frac{\lambda_{L1}\lambda_{L5}}{\lambda_{L5} - \lambda_{L1}} \right) (N_{L1}^i - N_{L5}^i) + m_{GF}^i + \varepsilon_{GF}^i = \lambda_w N_w^i + m_{GF}^i + \varepsilon_{GF}^i \quad (12)$$

$$\sigma_{GF}^2 = \left(\frac{\sigma_{\phi_{L1}}^2}{\lambda_{L1}^2} + \frac{\sigma_{\phi_{L5}}^2}{\lambda_{L5}^2} \right) + \left(\frac{\lambda_{L5} - \lambda_{L1}}{\lambda_{L5} + \lambda_{L1}} \right)^2 \left(\frac{\sigma_{\rho_{L1}}^2}{\lambda_{L1}^2} + \frac{\sigma_{\rho_{L5}}^2}{\lambda_{L5}^2} \right) \quad (13)$$

From the moment the UAS is activated and begins to receive GNSS code and carrier phase measurements, it will begin to calculate the Z_{GF} values for each individual satellite. These measurements are then filtered over a time interval T by taking a running average of all the measurements. Assuming the errors can be bounded by a FOGM process with a time constant τ , the variance of the filtered measurements for a given satellite can be described by the following equation:

$$\sigma_{GFF}^2 = \frac{2 * \sigma_{GF}^2}{T/\tau} - \frac{2 * \sigma_{GF}^2}{(\frac{T}{\tau})^2} (1 - e^{-T/\tau}). \quad (14)$$

The UAS will perform GFF for the duration of the operation up until initializing the EKF, while the reference station can perform GFF indefinitely, with the only constraint being the duration for which each maintains lock on a given satellite. When the UAS enters the service volume, the double differencing operation can be performed to obtain the double difference of the wide-lane integer ambiguity, as well as to eliminate any interfrequency biases.

$$\nabla \Delta \frac{Z_{GFF}^{i,j}}{\lambda_w} = \nabla \Delta N_w^{i,j} + \frac{m_{GFF}^{i,j}}{\lambda_w} + \frac{\varepsilon_{GFF}^{i,j}}{\lambda_w} \quad (15)$$

Lastly, for the first iteration of the Kalman filter, the $\nabla \Delta Z_{GFF}^{i,j}$ can be implemented into the measurement model to provide additional information on the cycle ambiguity states. The matrix combining this measurement and the double-differenced carrier phase is represented below (Khanafseh, 2008).

$$\begin{bmatrix} \nabla \Delta \bar{Z}_{GF} / \lambda_w \\ \nabla \Delta \phi_{L1} \\ \nabla \Delta \phi_{L2} \end{bmatrix} = \begin{bmatrix} \mathbf{0} & \mathbf{I} & -\mathbf{I} \\ \Delta \mathbf{e}_r^T & \lambda_{L1} \mathbf{I} & \mathbf{0} \\ \Delta \mathbf{e}_r^T & \mathbf{0} & \lambda_{L2} \mathbf{I} \end{bmatrix} \begin{bmatrix} \mathbf{x}_{ru} \\ \nabla \Delta \mathbf{N}_{L1} \\ \nabla \Delta \mathbf{N}_{L2} \end{bmatrix} + \begin{bmatrix} \varepsilon_{\nabla \Delta \bar{Z}_{GF}} \\ \varepsilon_{\nabla \Delta \phi_{L1}} \\ \varepsilon_{\nabla \Delta \phi_{L2}} \end{bmatrix} \quad (16)$$

The impact of geometry free filtering can be demonstrated clearly in Figure 3. The ratio of the uncertainty of the filtered double-differenced estimation (σ_{GFF}) to the unfiltered double-differenced estimation (σ_{GF}) is plotted against the non-dimensional

filtering time (T) divided by time constant value (τ). While the time correlation for multipath is based on the environment and is difficult to control, the amount of time the aircraft is allocated to perform GFF can be lengthened or shortened. Therefore, the performance of the system will depend significantly on how long the aircraft is allowed to perform geometry-free filtering.

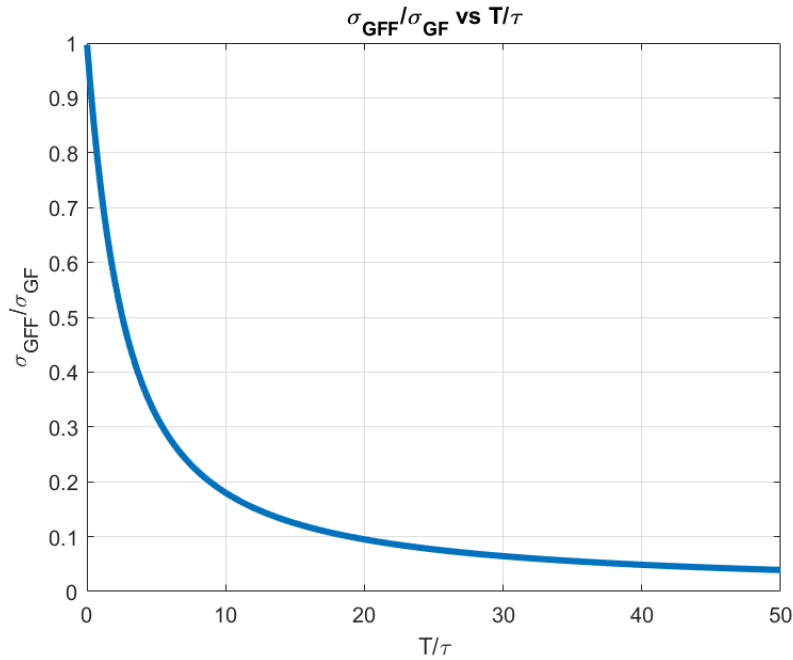


FIGURE 3 GFF Effect on Cycle Ambiguity Estimation

3.5 Extended Kalman Filtering With INS

The GNSS signals from the receiver and the reference station are processed in an EKF, which allows the system to achieve higher accuracy over time. The dynamic model of the EKF is tied to an inertial navigation system (INS). The INS has little effect on fault-free performance but helps bridge continuity gaps in the event of short-term GNSS interruptions (Nagai, 2025).

3.6 Zero-velocity Update

In the event the airplane starts at the gate, it does not need to perform GFF because it is within service volume, and the EKF has time to converge while stationary at the gate. The defining factor for the performance of the navigation system is the amount of time it requires to filter before achieving the positioning accuracy necessary to leave the gate. The performance of the EKF can be improved by implementing a zero-velocity update (ZUPT), which is a simulated measurement that the velocity of the airplane in the navigation frame is zero, with a chosen level of certainty. To maintain integrity, the actual movement of the aircraft must remain lower than the uncertainty reflected in the ZUPT. A dynamic model of the airplane during initialization and boarding/loading may need to be developed to determine what level of certainty is acceptable to use.

4. COVARIANCE ANALYSES

A covariance analysis was used to determine whether this implementation met the requirements. First, the GPS and Galileo satellite locations were propagated using week 906 of almanac data. These locations were used to calculate the line-of-sight vectors from the satellites to selected airport locations. The selected locations for the covariance analysis were Chicago O'Hare airport (41.98° N), Fairbanks, Alaska airport (64.82° N), and Hilo, Hawaii airport (19.72° N). The covariance analysis was further divided into different scenarios for departures, large aircraft landings, and small aircraft landings.

4.1 Departure

Since the aircraft starts within the service volume for the departure scenario, it does not need to implement GFF. However, the aircraft can take advantage of the GFF that has been done by the ground station previously, so it combines the ground station's cycle ambiguity calculations with its own unfiltered cycle ambiguity estimation. The airplane remains parked at the gate and must run the EKF until the horizontal positioning error (HPE) converges enough to allow the airplane to enter the taxiway while meeting the fault-free integrity requirement. Since the airplane is parked at the gate, the airport infrastructure may incur

some satellite blockages, and this is accounted for with a 30-degree elevation mask. The covariance analysis runs until the navigation system converges to provide positioning accuracy below the allowable taxilane HPE, and the time the EKF takes to converge to the taxilane entry requirement is recorded. Since the taxilane entry requirement is different according to each airport, the wait times were recorded for airports pertaining to ADG 1, ADG 2, and ADG 3. No ZUPT was implemented in the baseline departure simulations. Table 4 displays the parameters used in the simulation.

Parameter	Value	Parameter	Value
Code thermal noise (both receivers)	0.5 meters	Code multipath noise (both receivers)	0.75 meters
Carrier thermal noise (both receivers)	0.002 meters	Carrier multipath noise (both receivers)	0.01 meters
Ground station GFF time	8 hours (or as long as a satellite is visible)	Multipath time constant: Gate, Taxi, and Ground Station	120s
Aircraft GFF time	1 second	Ground station elevation mask	5 degrees

TABLE 4 Departure Covariance Analysis Parameters

The covariance analysis is repeated at 15-minute intervals over the course of 72 hours, for each of the airport locations being investigated. Figures 4A, 5A, and 6A show the wait time to meet a given accuracy on the y-axis and the start time of the simulation on the x-axis. Figures 4B, 5B, and 6B show the wait time to meet a given accuracy on the x-axis and the availability of meeting that given accuracy on the y-axis.

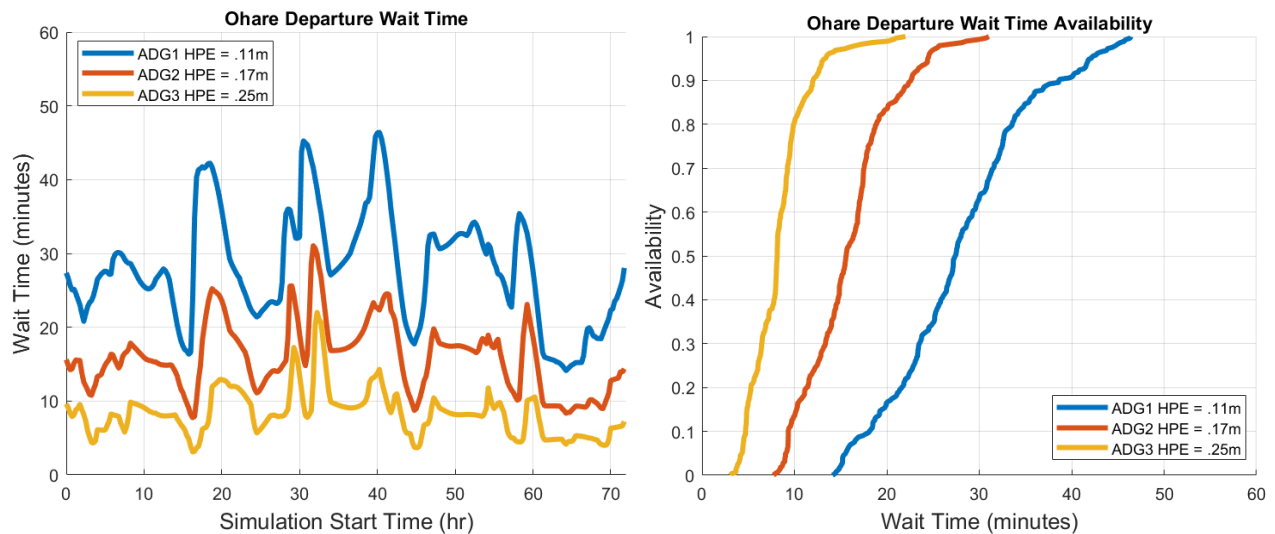


FIGURE 4. A) O'Hare Wait Time vs. Simulation Start Time, **B)** O'Hare Wait Time Availability

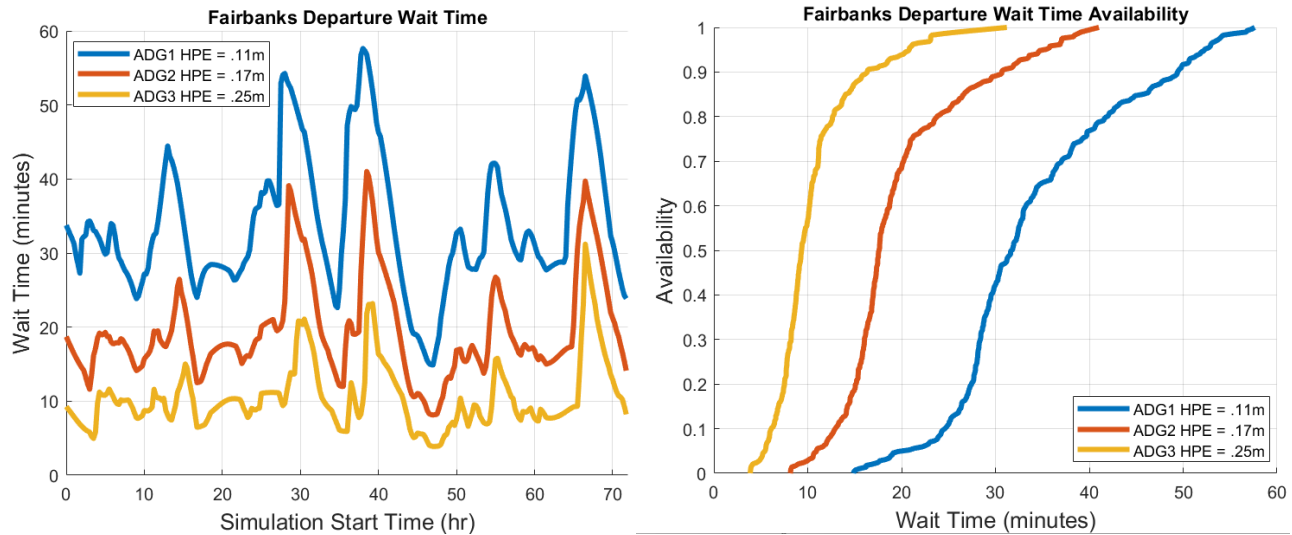


FIGURE 5. A) Fairbanks Wait Time vs. Simulation Start Time, B) Fairbanks Wait Time Availability

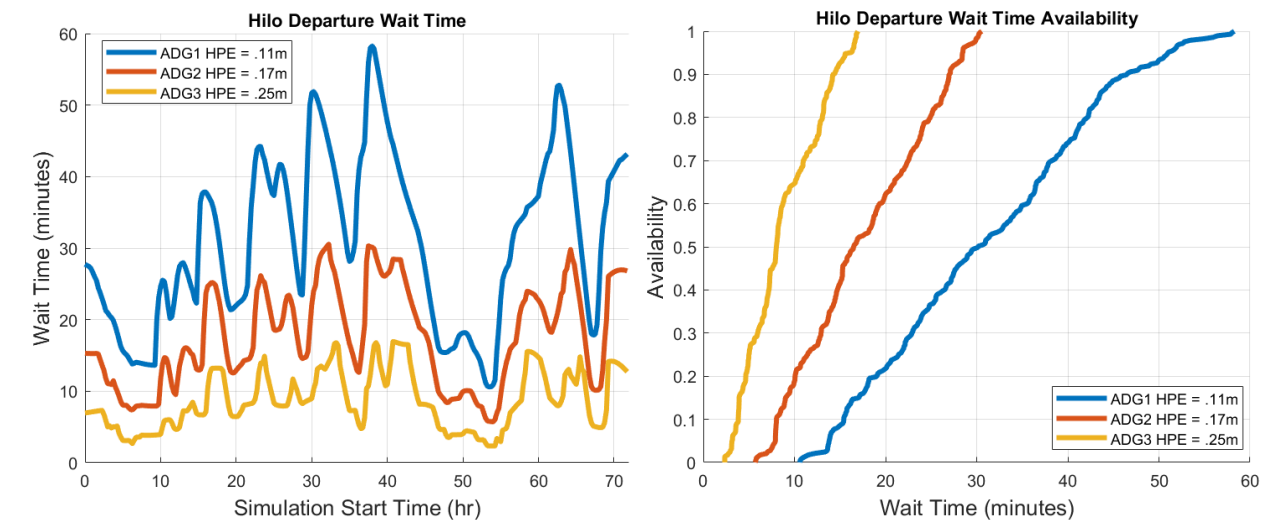


FIGURE 6. A) Hilo Wait Time vs. Simulation Start Time, B) Hilo Wait Time Availability

As the results show, the amount of time an aircraft will require to initialize and meet taxilane performance requirements depends heavily on the accuracy required and the location of the aircraft. In Fairbanks, the longest wait times for aircraft in ADG1, ADG2 and ADG 3 were 58 minutes, 41 minutes, and 32 minutes, respectively. At O’Hare, the same wait times were 47 minutes, 31 minutes, and 22 minutes, and at Hilo, the same wait times were 59 minutes, 31 minutes, and 17 minutes. Whether these waiting times are acceptable will be entirely dependent on the given user. If a user desires shorter wait times, initializing the aircraft where it has better satellite visibility, or implementing a ZUPT model may be two approaches to improve performance. Both approaches will be examined in the sensitivity analysis in Section 5.

4.2 Large Aircraft Arrival

Since ADG 3 is the smallest airport that a larger-sized aircraft could operate at, the covariance analysis results for large aircraft were compared with the ADG 3 accuracy requirements, which are the most stringent. Following figure 7 below, the UAS begins performing GFF during the gate initialization (1), taxi (2), and flight (3-5), for all satellites above 30 degrees. Even though the UAS starts within the service volume of the corrections, the UAS must leave the service volume during its flight and therefore begins GFF in anticipation of departing. Since the accuracy of the positioning system will be able to achieve increases with the amount of time the UAS is able to perform GFF, the shortest possible mission is considered. If the system is able to achieve enough accuracy assuming the shortest possible mission duration, it will be able to achieve enough accuracy for any duration of mission. In figure 7 below, we consider the shortest possible mission to be one where the UAS must make an unplanned return to the airport it departs from. Assuming that for the final approach (6) the aircraft maintains a bank angle

of less than 5 degrees, satellites between 5 and 30 degrees can also be filtered during that time. Once the aircraft lands (7), the EKF initializes and runs for the duration of rollout (8) until entry onto the normal taxiway (9). At that time, the horizontal positioning error of the navigation system was recorded to determine whether it would meet the taxiway operation (10) accuracy requirement at that instant. Before entering the taxilane (11), the horizontal positioning error (HPE) is recorded to determine whether the NSE would meet the taxilane operation (12) requirements at that instant. Along with recording the HPE from the EKF, a Least-Squares-Estimation (LSE) approach after touchdown was tested to see whether simpler implementation of the navigation system can be used, possibly making future integrity analysis easier. Table 4 displays the parameters used in the simulation.

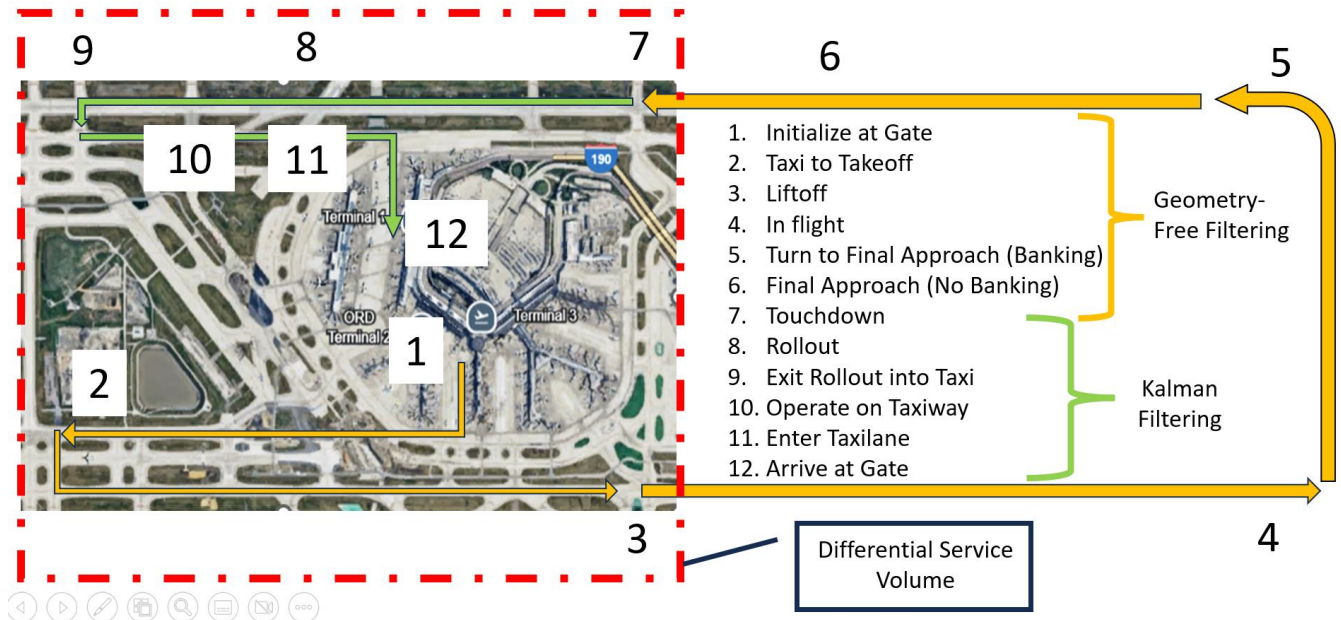


FIGURE 7 Aircraft Arrival Scenario

Parameter	Value	Parameter	Value
Gate Initialization Time	30 minutes	Code multipath noise (both receivers)	0.75 meters
Taxi Time	6 minutes	Carrier thermal noise (both receivers)	0.01 meters
Flight Time	10 minutes	In-flight multipath time constant	30 seconds
Elevation mask in Flight	30 degrees	Ground station filtering time	8 hours
Final Approach Time	3 minutes	Ground station elevation mask	5 degrees
Elevation mask Final Approach	5 degrees	Multipath time constant: Gate, Taxi, and Ground Station	120s
Code thermal noise (both receivers)	0.5 meters	Aircraft Rollout Time	30 seconds
Carrier thermal noise (both receivers)	0.002 meters	Aircraft Taxiway Time	120 seconds

TABLE 5 Large Aircraft Arrival Covariance Analysis Parameters

The covariance analysis for this scenario was run at 15-minute intervals over the course of 72 hours to allow for varying geometry combinations of GPS and Galileo. Figures 8, 9 and 10 show the standard deviation at taxiway and taxilane entry times on the y-axis and time of the simulation the x-axis for O’Hare, Fairbanks, and Hilo airports, respectively.

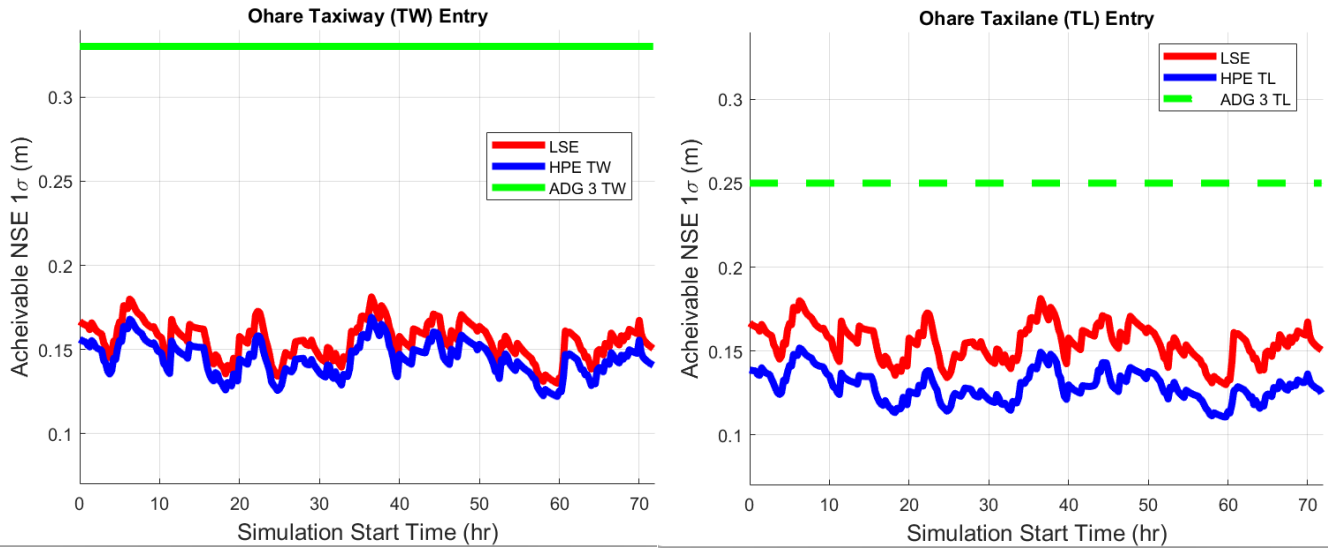


FIGURE 8 O'Hare Horizontal Positioning Error

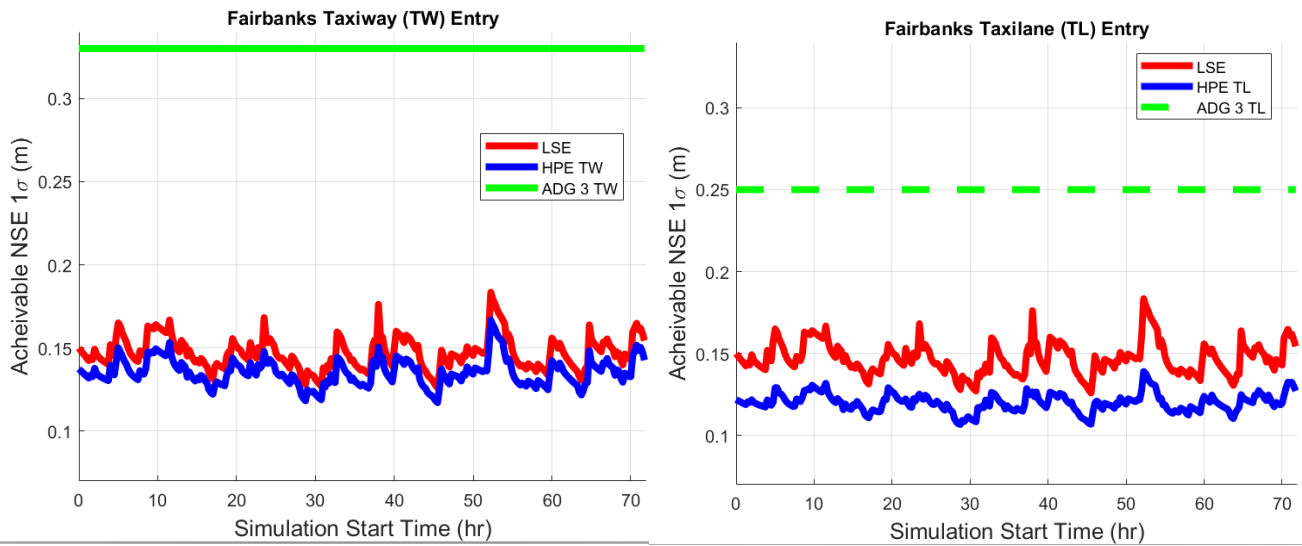


FIGURE 9 Fairbanks Horizontal Positioning Error

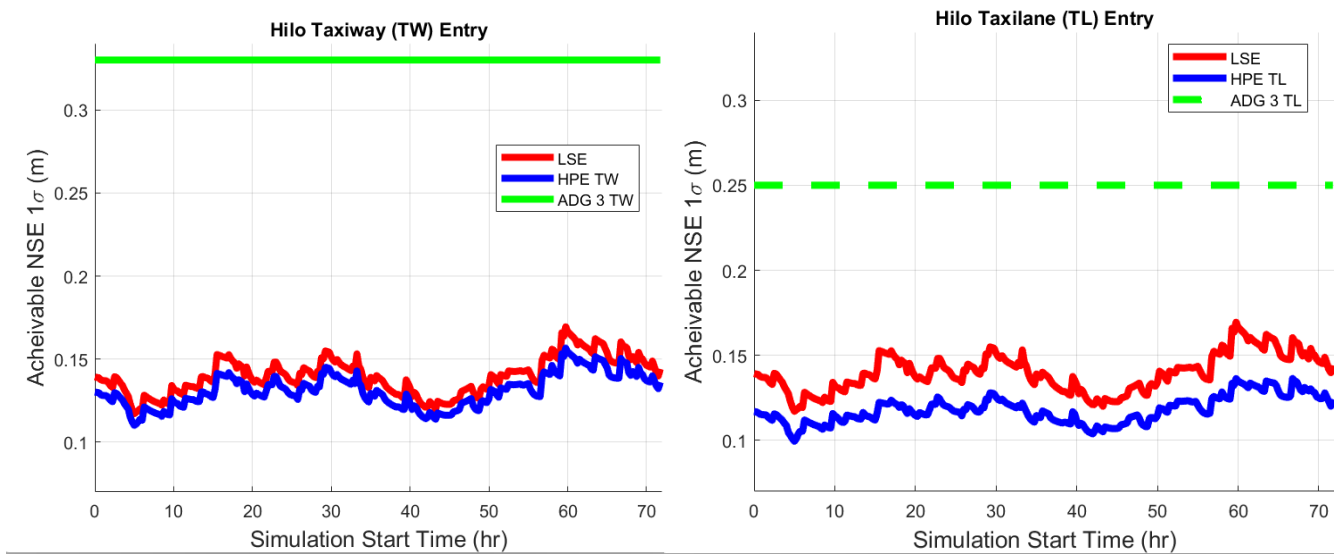


FIGURE 10 Hilo Horizontal Positioning Error

Figures 11, 12, and 13 show the availability on the y-axis vs 1-sigma accuracy achieved on the x-axis for the same three airports.

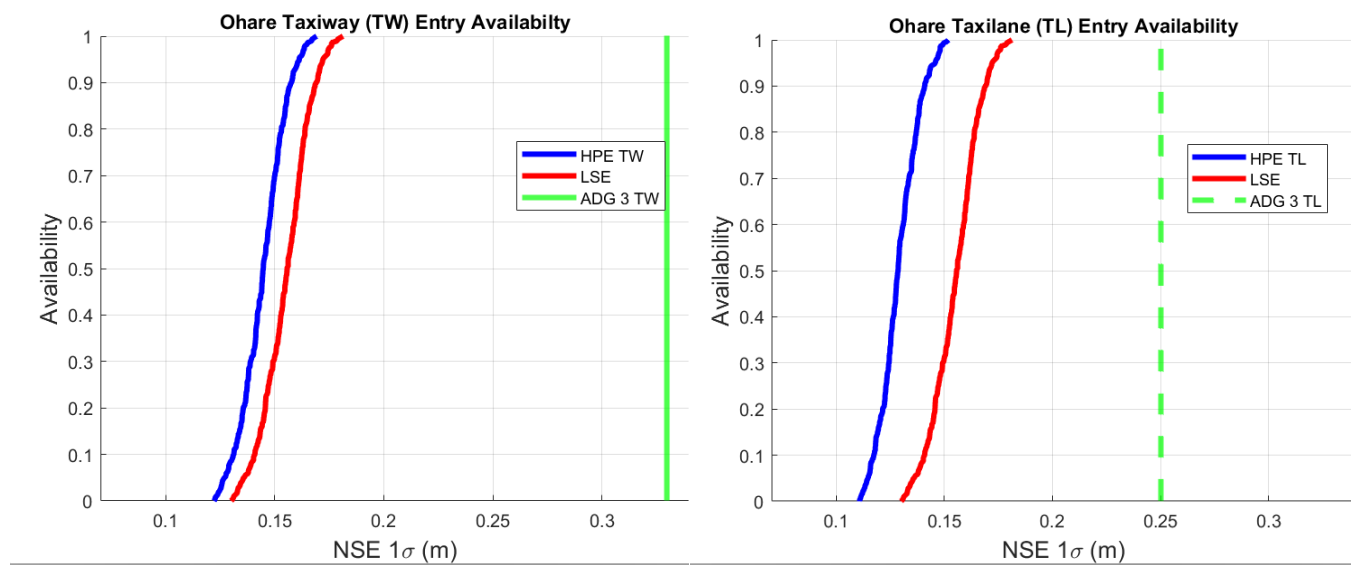


FIGURE 11 O'Hare Availability

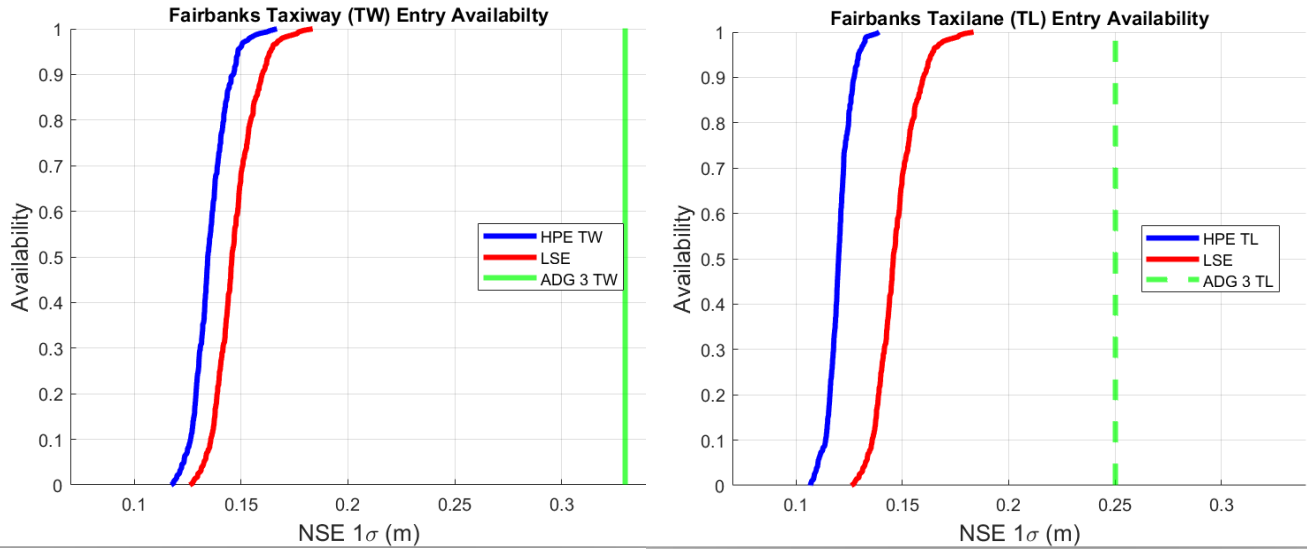


FIGURE 12 Fairbanks Availability

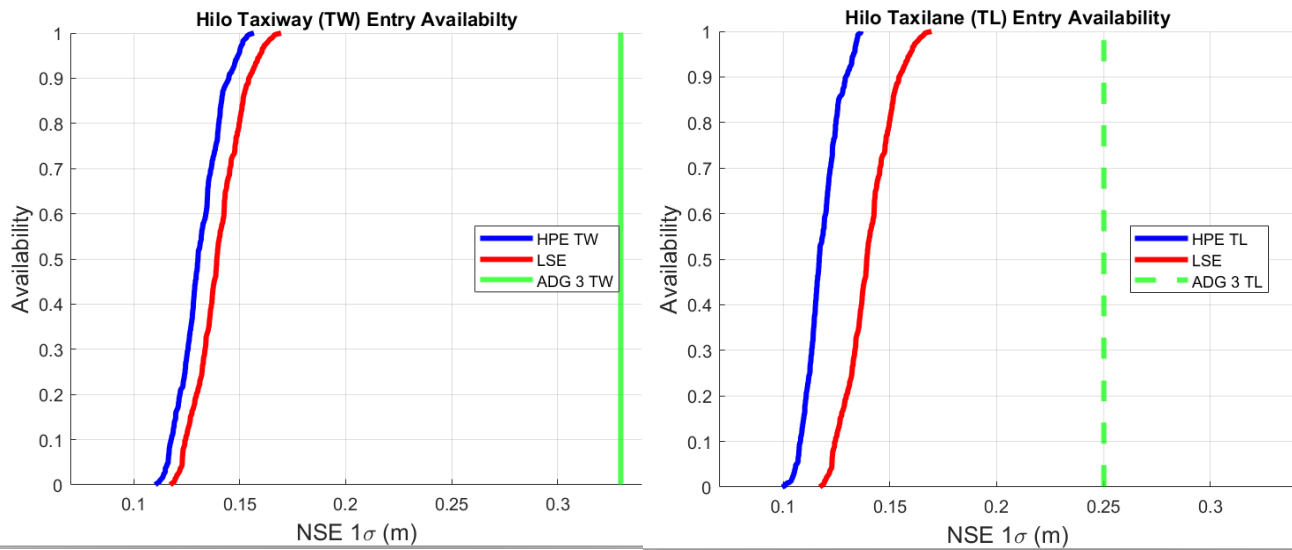


FIGURE 13 Hilo Availability

These results show that, at all locations, under the given fault-free requirements and assumed parameters, both the least-squares implementation and the Kalman filter provide 100% availability and exceed the requirements. A significant margin is available in case the multipath environment is worse than expected, the satellite visibility is worse than expected, the faulted scenario requires more budget, or the FTE needs more allocation. Future work will be dedicated to quantifying the multipath environment, developing better visibility models, and considering the possible faults that occur.

4.3 Small Aircraft Arrival

The small-aircraft arrival scenario is similar to the large aircraft arrival scenario, except for a few key parameters. The minimum taxi times, flight times, rollout times, and taxiway times are reduced. Additionally, since smaller aircraft experience faster oscillations, we use a multipath time constant of 5 seconds (Khanafseh, 2008). After the end of rollout, the HPE of the navigation system was recorded to determine whether it would meet the taxiway entry accuracy requirement at that instant. Before entering the taxilane the HPE is recorded to determine whether the NSE would meet the taxilane entry requirements at that instant. Along with recording the HPE from the EKF, the LSE approach after touchdown was tested to analyze whether simpler implementation of the navigation system can be used, possibly making future integrity analysis easier. Table 5 displays the parameters used in the simulation.

Parameter	Value	Parameter	Value
Gate Initialization Time	30 minutes	Code multipath noise (both receivers)	0.75 meters
Taxi Time	4 minutes	Carrier thermal noise (both receivers)	0.01 meters
Flight Time	5 minutes	In-flight multipath time constant	5 seconds
Elevation mask in Flight	30 degrees	Ground station filtering time	8 hours
Final Approach Time	45 seconds	Ground station elevation mask	5 degrees
Elevation mask Final Approach	5 degrees	Multipath time constant: Gate, Taxi, and Ground Station	120s
Code thermal noise (both receivers)	0.5 meters	Aircraft Rollout Time	10 seconds
Carrier thermal noise (both receivers)	0.002 meters	Aircraft Taxiway Time	60 seconds

TABLE 6 Small Aircraft Arrival Covariance Analysis Parameters

The covariance analysis for this scenario was repeated at 15-minute intervals over the course of 72 hours to allow for different geometric combinations of GPS and Galileo satellites. Figures 14, 15 and 16 show the standard deviation at taxiway and taxilane entry times on the y-axis and time of the simulation on the x-axis for the same three airports.

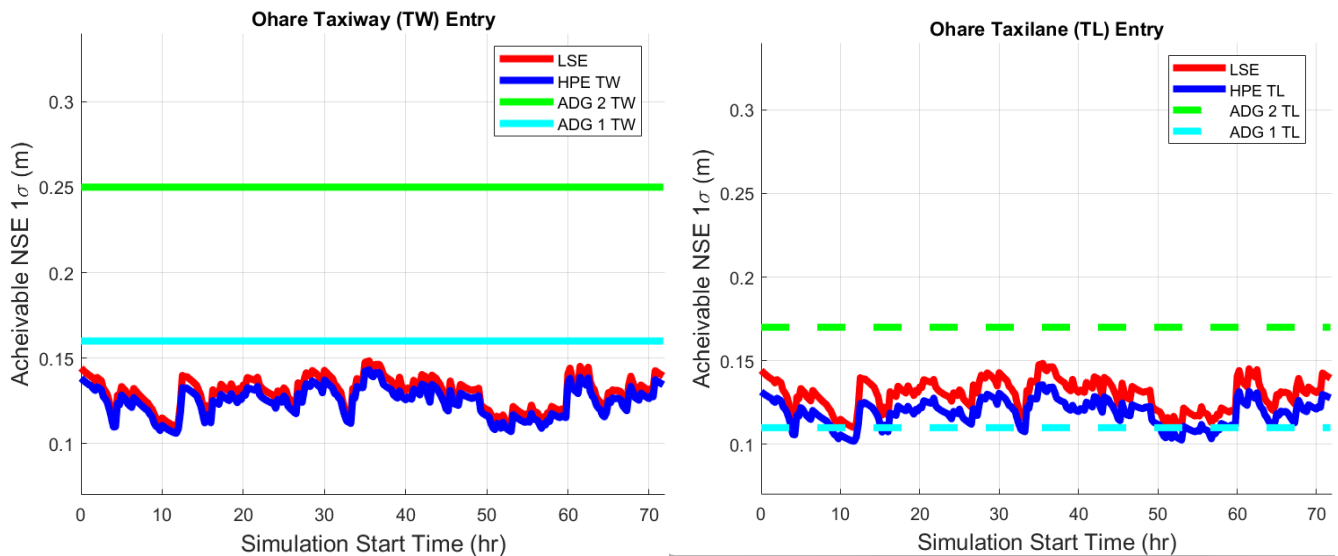


FIGURE 14 O'Hare Horizontal Positioning Error

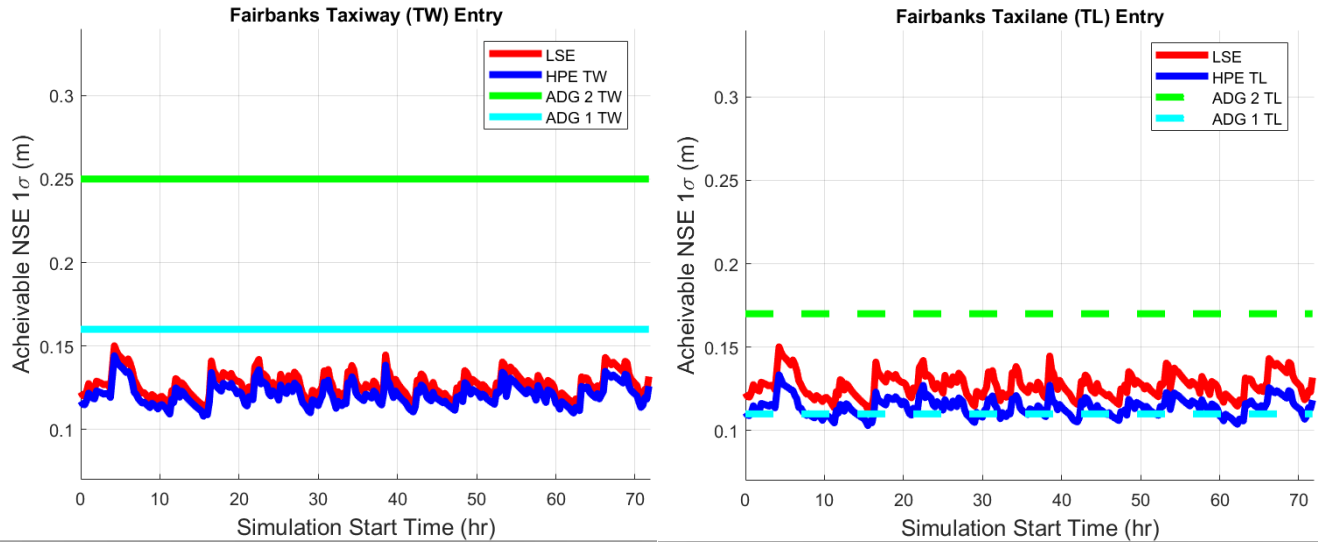


FIGURE 15 Fairbanks Horizontal Positioning Error

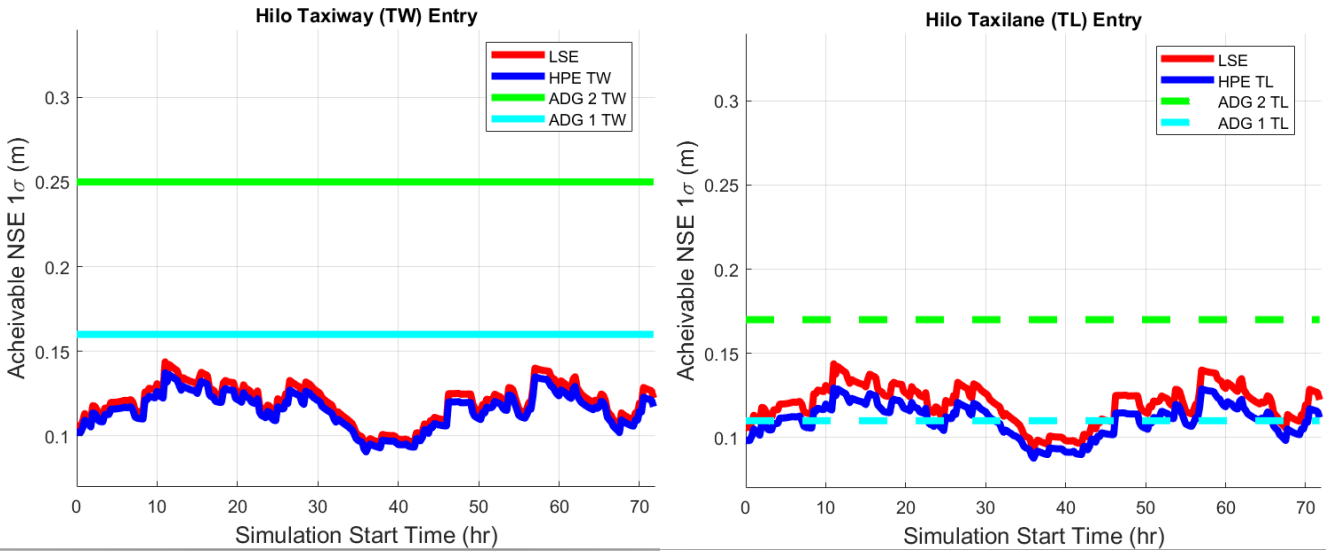


FIGURE 16 Hilo Horizontal Positioning Error

Figures 17, 18, and 19 show the availability on the y-axis vs 1-sigma accuracy achieved on the x-axis for the same airports.

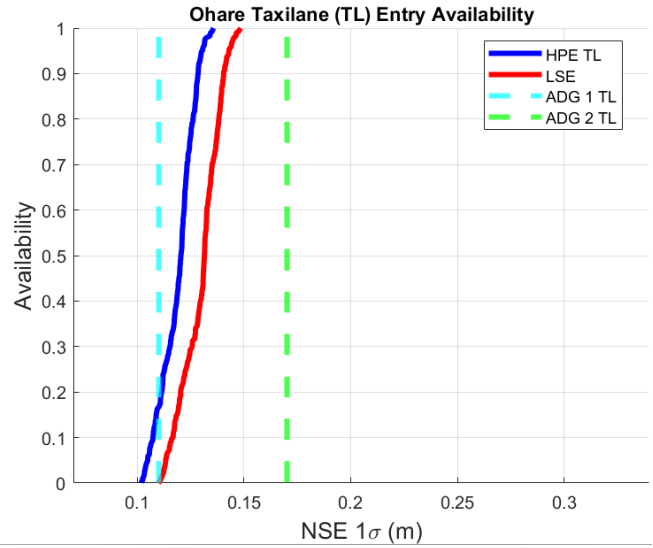
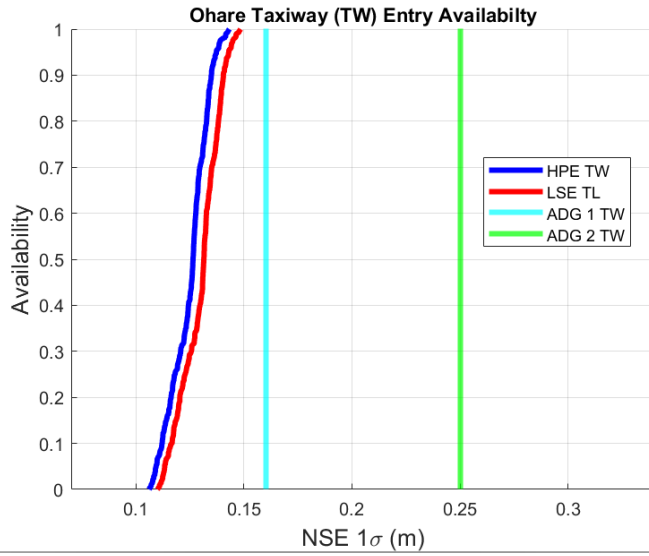


FIGURE 17 O'Hare Availability

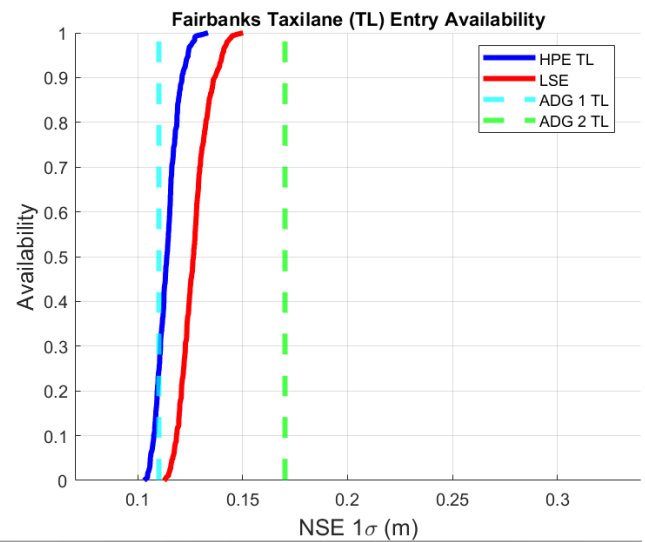
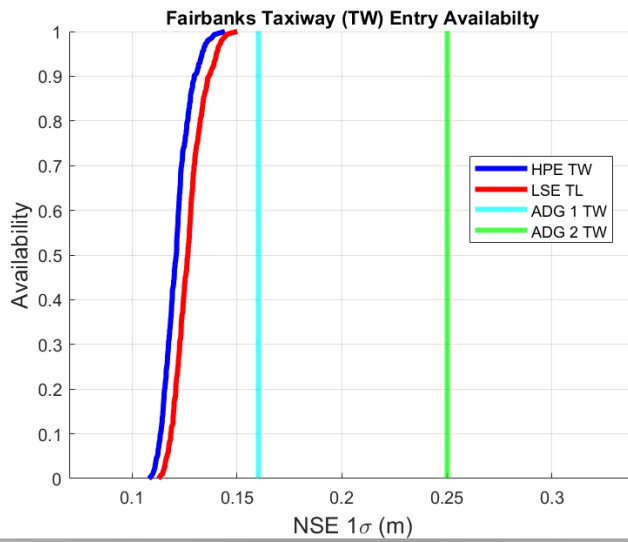


FIGURE 18 Fairbanks Availability

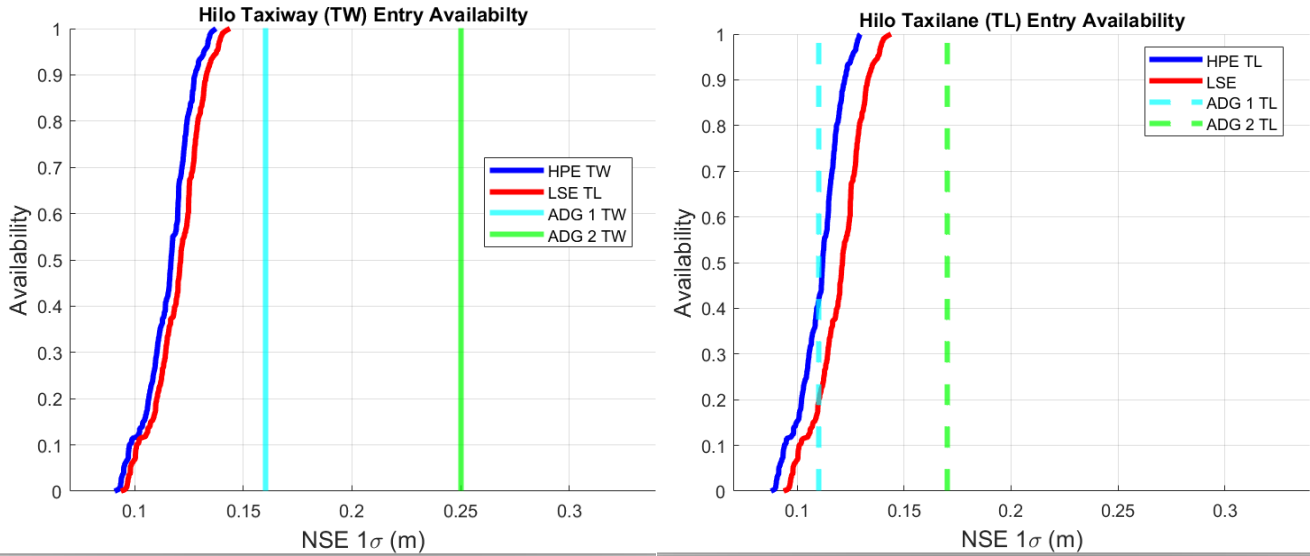


FIGURE 19 Hilo Availability

Figure 20 shows the availability plots zoomed in on the location of crossing ADG 1 TL accuracy requirement line.

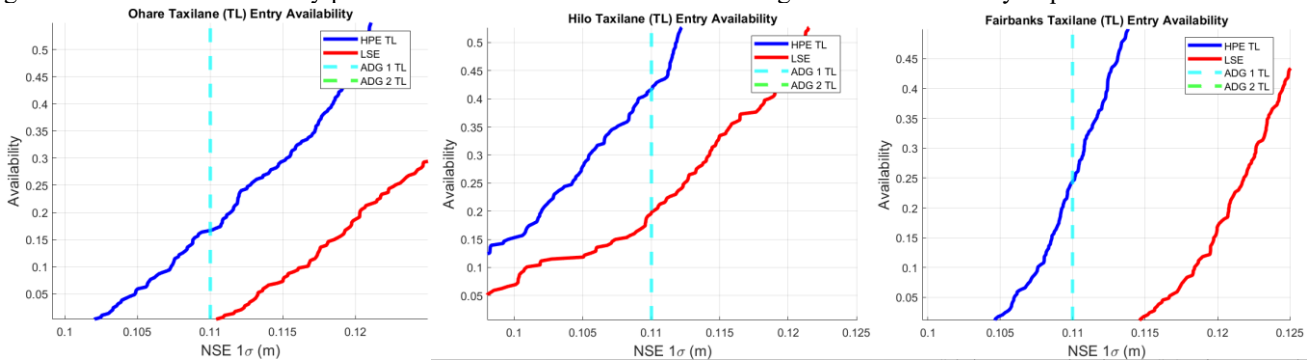


FIGURE 20 ADG 1 TL Availability Enlarged

These results show that, at all locations, under the given fault-free requirements and assumed parameters, both the LSE and the Kalman filter provide sufficient accuracy to meet the ADG 2 requirements with 100% availability. Therefore, the 10 seconds allocated to the EKF to initialize on the runway and the 60 seconds allocated to the EKF to initialize on the taxiway make little impact on meeting these requirements. Additionally, while the LSE and EKF provide enough accuracy to meet the ADG 1 taxiway entry requirements, neither system provides enough accuracy to meet ADG 1 taxilane entry requirements at any of the locations at even 45% availability. Therefore, this system is deemed to provide insufficient accuracy to operate on ADG 1 taxilanes. It remains to be determined whether a higher accuracy system should be pursued for operation in this space, since ADG 1 airports are uncommon and demand for UAS operation in this space may be quite low (A. Videmsek, personal communication, July 15, 2025). If UAS operation for these airports is desired, it may be possible to improve accuracy by allowing longer GFF times or pursue a higher accuracy system in future work.

5. SENSITIVITY ANALYSIS

A sensitivity analysis was performed to determine which parameters drive the performance of the system. Once these parameters are identified, further steps can be taken in future work to develop higher fidelity models. Additionally, the sensitivity analysis allows us to bring different tradeoffs to industry stakeholders and understand what approaches to improvement are viable within the aviation industry. Each sensitivity analysis was run by implementing a covariance analysis over 15-minute intervals across 72 hours at the O'Hare airport location. The sensitivity analysis investigated the impact of changing the thermal noise level for code measurements, the thermal noise level for carrier, the multipath noise level for code, the multipath noise level for carrier, the satellite blockage model, and the certainty of the ZUPT.

5.1 Thermal Noise

The impact of code thermal noise on the system was investigated using the small aircraft arrival scenario. Simulations were run using standard deviations of 0.5 m, 0.375 m, and 0.25 m, while keeping all other parameters the same. The average HPE using LSE and the EKF at taxiway entry and taxilane entry times was then determined for the 72-hour simulation duration.

Table 7 displays the results of the sensitivity analysis. Note that even when the code thermal noise was cut in half, the accuracy of the system at any of the locations was not reduced by even half of a centimeter. Since there is no time correlation, the thermal noise can be averaged over the duration of the GFF and the EKF, and its impact is almost negligible.

Code Thermal Noise	Horizontal Positioning Error 1 σ Least Squares Estimation	Horizontal Positioning Error 1 σ Taxiway Entry	Horizontal Positioning Error 1 σ Taxilane Entry
1 σ = 0.5m	0.1299	0.1249	0.1190
1 σ = 0.375m	0.1277	0.1238	0.1181
1 σ = 0.25m	0.1257	0.1231	0.1174

TABLE 7 Average Positioning Error Varying Code Thermal Noise

Next, the impact of carrier thermal noise was investigated in the same manner. Simulations were run using carrier thermal noise standard deviations of 2 mm, 1.5 mm, and 1 mm. The average HPE from the LSE and the EKF at taxiway entry and taxilane entry times was then determined for the 72-hour simulation duration.

Table 8 displays the results of the sensitivity analysis. Note that even when the carrier thermal noise was cut in half, the accuracy of the system at any of the locations was not reduced by even a millimeter. Since the carrier phase error is so much smaller than the thermal noise error, any change in the value is negligible with respect to the accuracy of the system.

Carrier Thermal Noise	Horizontal Positioning Error 1 σ Least Squares Estimation	Horizontal Positioning Error 1 σ Taxiway Entry	Horizontal Positioning Error 1 σ Taxilane Entry
1 σ = 0.002m	0.1299	0.1249	0.1190
1 σ = 0.0015m	0.1297	0.1248	0.1190
1 σ = 0.001m	0.1297	0.1248	0.1190

TABLE 8 Average Positioning Error Varying Carrier Thermal Noise

5.2 Multipath Noise

The impact of code multipath noise on the system was investigated using the small aircraft arrival scenario. Simulations were run using standard deviations of 1 m, 0.75 m, and 0.5 m, while keeping all other parameters the same. The average HPE using LSE and the EKF at the time of taxiway entry and taxilane entry was determined for the 72-hour simulation duration.

Table 9 displays the results of the sensitivity analysis. As can be seen, cutting the code multipath in half resulted in a significant increase in accuracy. This is expected if we revisit Equation 14, rewritten below as 14b.

$$\sigma_{GFF} = \sigma_{GF} \sqrt{\frac{2}{T/\alpha} - \frac{2}{(T/\alpha)^2} (1 - e^{-T/\alpha})} \quad (14b)$$

As long as the filtering time and time constant remain unchanged, any change in σ_{GF} results in a proportional change in σ_{GFF} by two. Although σ_{GF} is a combination of code and carrier noise, the carrier noise is sufficiently small that this value is largely dominated by code. Thus, any change in the standard deviation of the code multipath noise will be reflected proportionally in the change of σ_{GFF} .

Code Multipath Noise	Horizontal Positioning Error 1 σ Least Squares Estimation	Horizontal Positioning Error 1 σ Taxiway Entry	Horizontal Positioning Error 1 σ Taxilane Entry
1 σ = 0.1m	0.1657	0.1609	0.1521
1 σ = 0.75m	0.1299	0.1249	0.1190
1 σ = 0.5m	0.0958	0.0901	0.0859

TABLE 9 Average Positioning Error Varying Code Multipath Noise

As shown in Figure 21 below, the code multipath noise has a significant impact on whether this system can meet performance requirements for a given airport. In the flight and the airport environment, if the code has a standard deviation of 1 meter instead

of 0.75 meters, the availability for operating on ADG 1 TW drops from 100% to 38.7%, and the availability for operating on ADG 2 TL drops from 100% to 98.2%. On the other hand, if the code multipath has a standard deviation of 0.5 meters instead of 0.75 meters, the availability of entering ADG 1 TL rises from 16.4% to 100%. Therefore, having an accurate upper bound of the multipath code standard deviation is critical to maximizing the accuracy of the system while maintaining integrity.

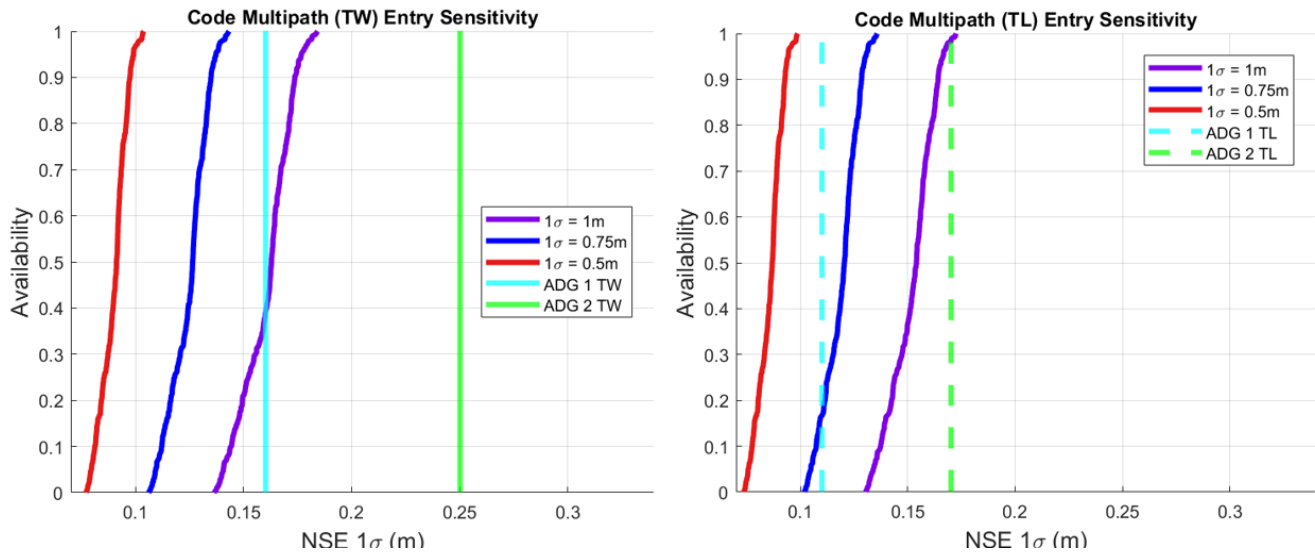


FIGURE 21 Code Multipath Sensitivity Availability

Next, the impact of carrier multipath noise was investigated in the same manner. Simulations were run using carrier multipath noise standard deviations of 1cm, 0.75cm, and 0.5cm. The average HPE using LSE and the EKF at taxiway entry and taxilane entry times was then determined for the 72-hour simulation duration.

Table 10 displays the results of the sensitivity analysis. While the carrier phase multipath noise had much less influence on the HPE than code multipath noise, it is interesting to note that the carrier phase has more influence the longer the EKF runs. Since the carrier phase provides improved accuracy with the changing line-of-sight vectors to the satellite, the carrier phase multipath noise can have an impact on the positioning accuracy of the EKF over longer periods of filtering.

Carrier Multipath Noise	Horizontal Positioning Error 1 σ Least Squares Estimation	Horizontal Positioning Error 1 σ Taxiway Entry	Horizontal Positioning Error 1 σ Taxilane Entry
1 σ = 0.01m	0.1299	0.1249	0.1190
1 σ = 0.0075m	0.1267	0.1218	0.1150
1 σ = 0.005m	0.1242	0.1192	0.1093

TABLE 10 Average Positioning Error Varying Carrier Multipath Noise

5.3 Satellite Blockage Model

We investigated the impact of the blockage model was investigated using both the small aircraft arrival and departure scenarios. For the arrival scenario, simulations were run using a maximum aircraft bank angle and building satellite blockage angle of 25 degrees, 30 degrees, and 35 degrees. The average HPE using LSE and the EKF at taxiway entry and taxilane entry times was then determined for the 72-hour simulation duration.

Table 11 displays the results of the sensitivity analysis. Since the satellite blockage model only impacts the GFF up to 45 seconds before the EKF is initialized, any effect that the changing elevation mask has on the EKF is due to the change in initial information provided by the GFF. While the change in HPE is minimal, reducing the bank angle that an aircraft would experience in-flight and ensuring that the blockage the aircraft has at the gate is no more than the maximum bank angle could provide slightly better availability if necessary.

Satellite Blockage Model	Horizontal Positioning Error 1 σ Least Squares Estimation	Horizontal Positioning Error 1 σ Taxiway Entry	Horizontal Positioning Error 1 σ Taxilane Entry
--------------------------	---	--	---

El mask = 35 deg	0.1382	0.1324	0.1257
El mask = 30 deg	0.1299	0.1249	0.1190
El mask = 25 deg	0.1222	0.1178	0.1126

TABLE 11 Satellite Blockage Sensitivity

For the departure scenario, the impact of the satellite blockage model on the initialization wait time was investigated. Covariance analyses were run at O’Hare, using elevation masks of 30, 20, and 10 degrees while keeping all other parameters constant. The maximum wait times for ADG/TDGs 1, 2 and 3 were recorded for each elevation mask. As shown below, since the margin for ADG 3 airports is larger, the initialization time is much lower. For larger aircraft that may take a long time to load, experiencing this length of initialization time should not be a problem. However, this could be an issue for users of smaller aircraft, for which it may take only a few minutes to load the aircraft and run through a pre-flight check list. If it is unacceptable to wait so long for the initialization process, reducing the satellite blockages by initializing in a more open-sky location would be a viable solution.

Satellite Blockage Model	ADG 1 (HPE $1\sigma = 0.11\text{m}$)	ADG 2 (HPE $1\sigma = 0.17\text{m}$)	ADG 3 (HPE $1\sigma = 0.25\text{m}$)
El mask = 30 deg	46 min 25 s	31 min 3 s	22 min 1s
El mask = 20 deg	32 min 11 s	17 min 28 s	8 min 44 s
El mask = 10 deg	19 min 25 s	9 min 13 s	3 min 40 s

TABLE 12 Departure Satellite Blockage Maximum Wait Time

5.4 ZUPT Model

We investigated the impact of the ZUPT model by feeding acceleration values of 0 into the dynamic model as accelerometer measurements. The certainty of these measurements was controlled by adjusting the level of uncertainty within the IMU itself. Replacing the IMU model with a constrained dynamic model of the aircraft during loading allows several variables to be controlled. The velocity random walk (VRW) can be correlated with any displacement the antenna might experience between the start and the end of loading, while the accelerometer bias stability (ABS) and the bias time constant can be correlated to the amplitude and frequency of oscillations due to the aircraft’s suspension system during loading. Table 13 displays the noise parameters used for both a typical IMU and a perfect zero-motion scenario. The LTAC IMU assumes the use of a Low-Tactical grade IMU but no ZUPT, while the perfect scenario represents the maximum possible improvement by assuming a perfectly static antenna. Future work can investigate what level of certainty is acceptable when implementing a ZUPT model.

IMU Name	LTAC	Perfect	Units
Velocity Random Walk	0.1	1×10^{-9}	Milli-g/sqrt (Hz)
Accelerometer Bias Stability	1	1×10^{-7}	Milli-g
Accelerometer Bias Time Constant	3600	0.5	Seconds

Table 13 Dynamic Model Parameters for ZUPT Sensitivity

Table 14 displays the maximum wait times at O’Hare airport under both dynamic models, with all other parameters unchanged from the departure scenario. A conservatively developed ZUPT model should provide significant improvement over the LTAC model but cannot provide a better wait time than the perfect model.

ADG/TDG	LTAC	Perfect
1, (HPE $1\sigma = 0.11\text{m}$)	46 min 25 s	17 min 44 s
2, (HPE $1\sigma = 0.17\text{m}$)	31 min 3 s	8 min 31 s
3, (HPE $1\sigma = 0.25\text{m}$)	22 min 1s	3 min 21 s

Table 14 Dynamic Model Maximum Wait Time

6. CONCLUSION

In this study, we focused on developing a navigation system that allows UAS to navigate on taxiways, taxilanes and runways. We propose using code-and-carrier differential GNSS, dual-constellation, dual-frequency, an EKF tightly coupled with an INS, augmented with Geometry-Free Filtering, and Zero-Velocity Update (ZUPT), to meet accuracy requirements. Results show that under the given assumptions and for the shortest possible arrival operations, the system can meet the horizontal positioning requirements in all locations. The system is even able to position under the most stringent requirements (TDG/ADG 1), assuming the multipath noise is not excessively high. Analysis also indicates that the accuracy of the system is heavily dependent on the code multipath noise. Additionally, under the departure scenario, the impact of the wait time is dependent on the satellite outages incurred by banking, size of the aircraft and airport, and zero-velocity update implemented. Future studies will focus on developing a multipath model for the aircraft and airport environments, performing integrity and continuity analyses, developing more-refined satellite blockage models, and developing a ZUPT model.

ACKNOWLEDGMENTS

This article is based on work performed for SurfNav4UAS supported by National Aeronautics and Space Administration (NASA) (Grant No. 80NSSC24M0069). The authors greatly appreciate the advice and help of Andrew Videmsek, Reliable Robotics Corporation and Sabrina Ugazio, Ohio University. Any opinions, findings, conclusions, or recommendations expressed in this paper are those of the authors and do not necessarily reflect the views of the sponsors.

REFERENCES

- Bang, E., Circiu, M.-S., Caizzone, S., Rippl, M., Garcia Crespillo, O. (2024). Effect of user antenna group delay variation error on advanced RAIM. *NAVIGATION*, 71(1). <https://doi.org/10.33012/navi.624>
- Davis, J. M. and Kelly, R. J. (1993). RNP tunnel concept for precision approach with GNSS application. In *Proceedings of the 1993 Annual Meeting of The Institute of Navigation*, pages 135–154.
- Felux, Michael, Nietlispach, Michael, "From Ground to Air: The Paradigm Shift in GBAS Monitoring and Its Benefits," *Proceedings of the 2025 International Technical Meeting of The Institute of Navigation*, Long Beach, California, January 2025, pp. 305-317. <https://doi.org/10.33012/2025.19962>
- Heo, M.-B., & Pervan, B. (2006). Carrier phase navigation architecture for shipboard relative GPS. *IEEE Transactions on Aerospace and Electronic Systems*, 42(2), 527–540. <https://doi.org/10.1109/TAES.2006.1642580>
- International Civil Aviation Organization. (1999). *Annex 14 to the Convention on International Civil Aviation: Aerodromes (3rd ed.)*.
- Khanafseh, S. (2008). *GPS navigation algorithms for autonomous airborne refueling of unmanned air vehicles* (Doctoral dissertation, Illinois Institute of Technology). <http://www.navlab.iit.edu/list-by-year.html>
- Nagai, K. (2025). Integrity of urban driverless vehicle navigation with multi-sensor integration [Doctoral dissertation, Illinois Institute of Technology]. http://www.navlab.iit.edu/uploads/5/9/7/3/59735535/kana_thesis.pdf.
- Pervan, B., Khanafseh, S., & Patel, J. (2017). Test statistic auto- and cross-correlation effects on monitor false alert and missed detection probabilities. In *Proceedings of the 2017 International Technical Meeting of the Institute of Navigation (ION ITM)*, Monterey, CA, January 2017.
- RTCA SC-159. (1999, January 7). *The role of the global navigation satellite system (GNSS) in supporting airport surface operations (RTCA/DO-247)*.
- Schuster, W., & Ochieng, W. (2011). Airport surface movement – Critical analysis of navigation system performance requirements. *Journal of Navigation*, 64(2), 281–294. <https://doi.org/10.1017/S0373463310000236>
- Song, J., Milner, C., & No, H. (2024). Feasibility study of GBAS/INS and RRAIM for airport surface movement under low-visibility conditions. *NAVIGATION*, 71(4). <https://doi.org/10.33012/navi.673>
- U.S. Department of Transportation, Federal Aviation Administration. (2024, August 16). *Airport design* (Advisory Circular No. 150/5300-13B). <https://www.faa.gov/>